

Article

DFT Investigation of the Molecular Properties of the Dimethylglyoximato Complexes $[M(\text{Hdmg})_2]$ ($M = \text{Ni}, \text{Pd}, \text{Pt}$)

Maryam Niazi and Axel Klein * 

Department of Chemistry, Faculty for Mathematics and Natural Sciences, Institute for Inorganic Chemistry, University of Cologne, GreinstraÙe 6, D-50939 Köln, Germany; mniazi@uni-koeln.de

* Correspondence: axel.klein@uni-koeln.de

Abstract: Important applications of the Ni^{II} , Pd^{II} and Pt^{II} complexes $[M(\text{Hdmg})_2]$ (H_2dmg = dimethylglyoxime) stem from their metal...metal stacked virtually insoluble aggregates. Given the virtual insolubility of the materials, we postulated that the rare reports on dissolved species in solution do not represent monomolecular species but oligomers. We thus studied the structural and spectral properties of the monomolecular entities of these compounds using density functional theory (DFT) and time-dependent DFT computations in dimethyl sulfoxide (DMSO) as a solvent. The molecular geometries, IR and UV-vis spectra, and frontier orbitals properties were computed using LANL2DZ ecp and def2TZVP as basis sets and M06-2X as the functional. The results are compared with the available experimental and other calculated data. The optimised molecular geometries proved the asymmetric character of the two formed $\text{O}-\text{H}\cdots\text{O}$ bonds which connect the two Hdmg^- ligands in the completely planar molecules. Calculated UV-vis spectra revealed the presence of three absorptions in the range 180 to 350 nm that are red-shifted along the series Ni–Pd–Pt. They were assigned to essentially ligand-centred $\pi-\pi^*$ transitions in part with metal(d) to ligand(π^*) charge transfer (MLCT) contributions. The notorious d-p transitions dominating the colour and electronics of the compounds in the solid-state and oligomeric stacks are negligible in our monomolecular models strongly supporting the idea that the previously reported spectroscopic observations or biological effects in solutions are not due to monomolecular complexes but rather to oligomeric dissolved species.

Keywords: Ni^{II} ; Pd^{II} ; Pt^{II} ; dimethylglyoxime; DFT



Citation: Niazi, M.; Klein, A. DFT Investigation of the Molecular Properties of the Dimethylglyoximato Complexes $[M(\text{Hdmg})_2]$ ($M = \text{Ni}, \text{Pd}, \text{Pt}$). *Inorganics* **2021**, *9*, 47. <https://doi.org/10.3390/inorganics9060047>

Academic Editor: Yi Luo

Received: 27 April 2021

Accepted: 29 May 2021

Published: 7 June 2021

Publisher's Note: MDPI stays neutral with regard to jurisdictional claims in published maps and institutional affiliations.



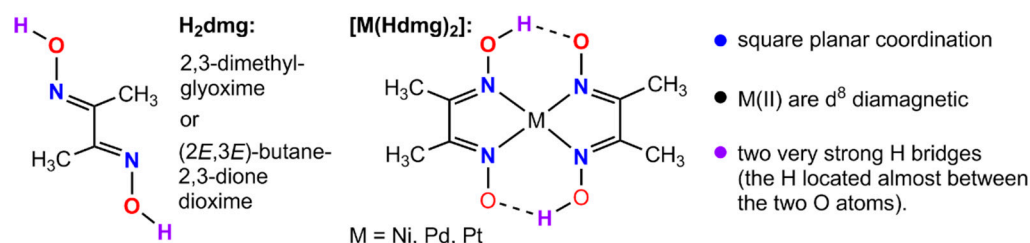
Copyright: © 2021 by the authors. Licensee MDPI, Basel, Switzerland. This article is an open access article distributed under the terms and conditions of the Creative Commons Attribution (CC BY) license (<https://creativecommons.org/licenses/by/4.0/>).

1. Introduction

The three compounds $[M(\text{Hdmg})_2]$ ($M = \text{Pt}, \text{Pd}, \text{Ni}$) owe most of their specific properties to the peculiar dimethylglyoximato ligand Hdmg^- (= singly deprotonated 2,3-butane-2,3-dione dioxime) [1–25]. Two Hdmg^- ligands in a square planar coordination allows two very strong $\text{O}-\text{H}\cdots\text{O}^-$ hydrogen bonds (H bonds) of the two neighbouring oxime and oximate functions (Scheme 1) and the localisation of the proton was discussed as to lie close to a symmetric H bond [1–5,9–13,21,24]. As a result of these H bonds, the Ni^{II} complex is square planar.

Contrary to an earlier report which considered the short H bond in $[\text{Ni}(\text{Hdmg})_2]$ as responsible for the low solubility [24], $\text{Ni}\cdots\text{Ni}$ stacking interactions of the square planar structures are causing effective aggregation and low solubility in various solvents in line with the slightly higher solubility of the ethylmethylglyoximate $[\text{Ni}(\text{Hemg})_2]$ and other derivatives [9,10,15,18,23]. Even though $[\text{Ni}(\text{Hemg})_2]$ has a shorter $\text{O}\cdots\text{O}$ distance of 2.33 Å [18] compared with $[\text{Ni}(\text{Hdmg})_2]$ (2.40 Å or longer; Table S1) and probably stronger hydrogen bonding, the solubility is markedly higher. The poor solubility alongside the bright red colour is well-established as a probe for Ni^{II} in elemental analyses [16,17,22,23]. Even without the H bonds, the geometry of the Pd^{II} and Pt^{II} derivatives would be square planar, due to the intrinsically strong ligand field of 4d and 5d metals, and the metal...metal stacking

is facilitated for these two elements due to the larger size of their frontier d orbitals [9]. Thus, all three complexes form extensive stacks with relatively short M...M distances of 3.24 (Ni) [4,10,11,14,19,24], 3.25 (Pd) [13,19], or 3.26 Å (Pt) [10,12,13,20], respectively in their solid structures with neighbouring molecules being rotated by almost 90° to allow room for the CH₃ groups (collected structural data in Table S1, Supplementary Materials).



Scheme 1. Schematic sketch of the three complexes $[M(\text{Hdmg})_2]$.

Pressure experiments have shown that the M...M interactions account also for the compressibility of these structures and the pressure-dependent changes of colour and electronic properties [3,4,8,12,26–31]. These virtually insoluble metal...metal stacked solids are the basis for applications of the three compounds $[M(\text{Hdmg})_2]$ ($M = \text{Pt}, \text{Pd}, \text{Ni}$) for the extraction or removal of these elements [32–35], as components of solid catalysts [36–40], as solid but easily evaporable precursors [37–47], and in optical devices (e.g., pressure calibrants/indicators) [3,4,12,26–31,48–51].

On the other hand, some applications as the analytical photometric determination of traces of Ni, Pd or Pt [32,35,52] or their use in (medical) coordination chemistry [52–56] seem to make use of the properties of the molecular units and UV-vis absorption spectra of $[\text{Ni}(\text{Hdmg})_2]$ in solution have been discussed as to stem from monomolecular units [15,16,46,57]. However, other spectroscopic data from species in solution is not reported and the frequently reported virtual insolubility of the materials sheds doubts on the question of the monomolecular species cause the absorptions of $[\text{Ni}(\text{Hdmg})_2]$ [15,16,52,57] and are responsible for the biological effects of $[\text{Ni}(\text{Hdmg})_2]$ [53] and $[\text{Pt}(\text{Hdmg})_2]$ [54]. Recent quantum chemical calculations on $[\text{Ni}(\text{Hdmg})_2]$ gave absorption bands at 180, 220, 248sh, and 359 nm for the monomer and marked shifted bands (183, 218, 254sh, 368 nm) for the dimer in the gas phase letting us assume that the reported solution spectra represent dissolved, but very probably oligomeric species.

We thus embarked on a study of the three complexes $[M(\text{Hdmg})_2]$ ($M = \text{Ni}, \text{Pd}, \text{Pt}$) using density functional theory (DFT). Starting from the results of the previous DFT study on the $[\text{Ni}(\text{Hdmg})_2]$ complex, which used the range-separated hybrid functional $\omega\text{B97X-D}$, augmented with dispersion correction and split-valence LANL2DZ effective core potentials (ecp) for Ni and 6-31G (d,p) basis set for all non-metallic elements [1], we chose the M06-2X as nonlocal functional without any symmetry constraint and split-valence LANL2DZ ecp (all metals) and def2TZVP (other atoms) basis sets. In contrast to the previous calculation that was carried out in the gas-phase, we applied the conductor-like polarizable continuum model (CPCM) for DMSO as a solvent to study the effect of this very polar solvent in comparison to the non-polar gas-phase study. The def2TZVP basis set instead of the more sophisticated 6-31G (d,p) was chosen to save computational time. For the same reason, we used the Hay and Wadt effective core potentials for the metal atoms. We thus calculated molecular structures, IR data, frontier orbital compositions, and UV-vis absorption spectra. We compared our calculated results with available experimental data and results from similar DFT studies with different functionals and basis sets and thus also provide an overview of the present state of knowledge.

Recently reported DFT and TD-DFT calculations on the molecular and electronic structures of planar d^8 configured Ni^{II} , Pd^{II} , and Pt^{II} complexes have shown that the reliability of calculated data with experimental data [58–66] is very much dependent on functionals and basis sets. Furthermore, comparative DFT and experimental studies for

these three metals were recently reported [62–67] allowing to gauge for the differences of these three metals.

2. Experimental Section

Computational Methods. All calculations were performed using the Gaussian 09 suite of programs [68]. Geometry optimisations and calculations of all complexes were carried out in DMSO as solvent using density functional theory (DFT) employing the conductor-like polarizable continuum model (CPCM) [69,70]. The functional for this study is M06-2X [71] as nonlocal functional, which is applied without any symmetry constraint. We used split-valence basis sets def2TZVP [72] for all non-metallic elements and LANL2DZ [73] for metals (M = Ni, Pd, and Pt) the latter applying the effective core potentials ecp(10/18) for Ni, ecp(28/18) for Pd, and ecp(60/18) for Pt by Hay and Wadt [74–76]. TD-DFT calculations for UV-vis transitions were run at the same level of theory and basis sets with DMSO as a solvent model for 45 singlet excited states.

3. Results and Discussion

3.1. DFT-Optimised Molecular Geometries

The DFT-calculated geometries show centrosymmetric planar molecules with two identical O–H···O bonds (Figure 1). In contrast to earlier reports [4,5,12,15,18] we did not find different torsion angles of the four CH₃ groups. In a recent experimental diffraction study using high-quality single crystals of [Ni(Hdmg)₂] up to pressures of 5 GPa [4] interactions with the two different oxime O atoms on one Hdmg[−] ligand led to different torsion angles of the two CH₃ groups. We suppose that our calculations underestimate these small torsional energies [4].

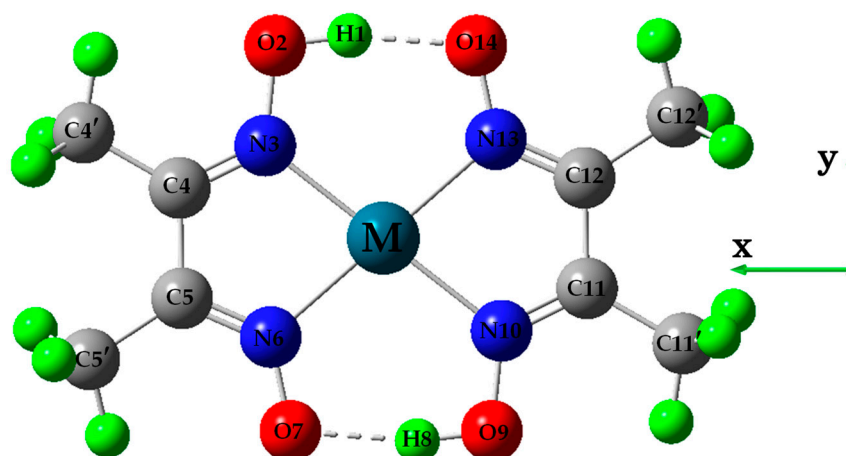


Figure 1. General schematic of the structures of [M(Hdmg)₂] (M = Ni, Pd, Pt), with numbering.

The calculated M–N bond lengths increase from 1.912 to 2.015 Å along the series Ni << Pt < Pd which reflects the size of the central atom (Tables S2–S4, Supplementary). In many experimental and theoretical studies, Pd^{II} has been found slightly larger than Pt^{II} [63–66,77–81], in keeping with the effects of the lanthanide contraction [82]. While for the Ni complex (Table S2) the two calculated M–N bonds show identical length, for Pd the M–N6(oximate) bond is slightly shorter than M–N3(oxime) (Table S3). For Pt M–N3 is markedly shorter than M–N6 (Table S4). Experimentally M–N6 is found slightly shorter than M–N3 for both Pt and Pd, while for Ni the experimental data is ambiguous. A shorter M–N6 bond compared to the M–N3 bond is in line with a Coulombic contribution to the M–L bond which is probably not correctly reproduced by the DFT calculations which usually overestimate the covalent character of a bond.

The oxime/oximate N3–O2/N6–O7 bonds are calculated in excellent agreement with the experimental values showing a markedly shorter N6–O7 bonds in all cases. Also

the chelate N3–M–N6 angles about 82° for the Ni complex and ~79° for the Pt and Pd derivatives agree very well with the experimental data. The same is true for the N6–M–N10 angles (~97° for Ni; ~100 for Pd and Pt) which, together with the size of the metal set the stage for the O–H···O hydrogen bond (Figure 1).

In agreement with the experimental data, the computations reproduced the strong asymmetric O–H···O hydrogen bonds [83]. Most of our calculated geometries of these H bonds agree very well with the experimental data. The maximum differences between recent X-ray data [4,11] and our results for Ni complex in angles and bond lengths are just 2.4° and 0.1 Å, respectively. As expected the O···H distance increases from Ni (1.45 Å) to Pt (1.67 Å) and Pd (1.70 Å) in keeping with the increasing ionic radii. The O–H bond length decreased slightly from 1.05 (Ni) to 1.01 Å (Pd and Pt). Both findings agree also very well with IR data (see later) and the markedly weaker H bonds in [Pd(Hdmg)₂] and [Pt(Hdmg)₂] were supported by both previous X-ray diffraction [12,13] and computational studies [1,3,5].

The essence of the O–H···O bond in [Ni(Hdmg)₂] has been under debate. Some early X-ray diffraction and spectroscopic studies [16,20,24,84,85], suggested a symmetric H bond in which the H atoms occupies a central position between the two O atoms and a very recent theoretical study found a symmetric relaxed potential energy curve (PEC) [1]. However, the same DFT study could show that the rigid PEC exhibits asymmetric double-well potentials with two clear minima [1] in keeping with other experimental work from 1959 to date [11,19,28,86–90], and further theoretical studies [3,5], thus proving the asymmetric nature of the mentioned bond. Our calculated O–H and O···H geometries showed the clear orientation of the proton towards one of the oxygen atoms and thus a clearly unsymmetric H bond.

It is interesting to note that previous calculations on the molecular geometries of the isolated [M(Hdmg)₂] complexes (M = Ni, Pd, Pt) using B3P86 exchange-correlation density functional in conjunction with a 6-311+(+)G** basis set (in the gas phase) [5] gave generally shorter M–N bonds, slightly shorter N–O bonds, very similar N–M–N angles and rather identical geometries for the O–H···O hydrogen bond and their surroundings compared with our data calculated with the M06-2X functional LANL2DZ ecp and def2TZVP as basis sets in DMSO solution. The authors of this study report that the values calculated with the B3LYP functional gave lower agreement with experimental data. However, the main problem is that experimental data is only available for the stacked molecules in the solid making comparison with data calculated in the gas phase [5] or in solution (our study) impossible. In a very recent study on [M(Hdmg)₂] (M = Ni, Cu), the range-separated hybrid functional ωB97X-D, augmented with dispersion correction, was used alongside with split-valence 6-31G (d,p) basis set for all non-metallic elements and LANL2DZ ecp for Ni and Cu [1]. The geometry of the [Ni(Hdmg)₂] complex does not vary largely from ours. This method allowed also to calculate the Ni···Ni distances to 3.17 Å, which is markedly shorter than the reported experimental values of about 3.24 Å (Table S1) [1]. In a similar way, the Pt derivative [Pt(Hdmg)₂] was geometry-optimised using the mPW1PW91 functional with 6-31G(d,p) and LANL2DZ basis sets, again with very similar molecular geometries [3]. The Pt···Pt distance at ambient pressure was calculated to 3.3 Å which compares reasonably well with about 3.25 Å found in experimental structures (Table S1).

3.2. Infrared (IR) Spectroscopy

The DFT-calculated IR spectra of [M(Hdmg)₂] (M = Ni, Pd, Pt) complexes contain characteristic absorption bands for the O–H, C=N, and N–O vibrations (Figure 2).

Our spectral assignments (Tables 1–3) are in keeping with an early detailed report on the IR spectra of Ni-, Pd-, Pt- and Cu-dimethylglyoximate complexes, including deuteration experiments [21], DFT-calculated and experimental data on [Ni(Hdmg)₂] [87], and recent DFT-calculated IR spectra for [Ni(Hdmg)₂] [1]. The marked deviation of the calculated values from experimental data is very probably because all these experiments have been carried out on solid samples. Thus, the experimental data represents the molecular stacks

and not isolated molecules. Therefore, instead of comparing our calculated data with experimental data, we use it solely for benchmarking our computational method.

Compared with the recently applied range-separated hybrid functional ω B97X-D, augmented with dispersion correction and split-valence 6-31G (d,p) basis set for all non-metallic elements and LANL2DZ ecp [1], our results for the N-O stretching vibration of the $[\text{Ni}(\text{Hdmg})_2]$ gave markedly lower values, while the C=N stretch are quite similar and the O-H bending is calculated at far higher energy (Table 1). Compared with the results from early calculations using the B3LYP functional and 6-311+(+)G**basis set for all atoms [87] our introduction of split basis had only a small impact on the N-O stretching and O-H bending energies, while for the C=N stretch our values lie markedly higher. Compared with the experimental data from solid samples, our calculated values and those of the recent DFT study using also split basis sets [1] are much higher. We tentatively ascribe this to the more sophisticated modelling of the metal atoms using split basis sets and believe that values of about 1650 cm^{-1} represent the C=N stretch in isolated molecules, while the stacking in the solid reduces the energy of this resonance markedly.

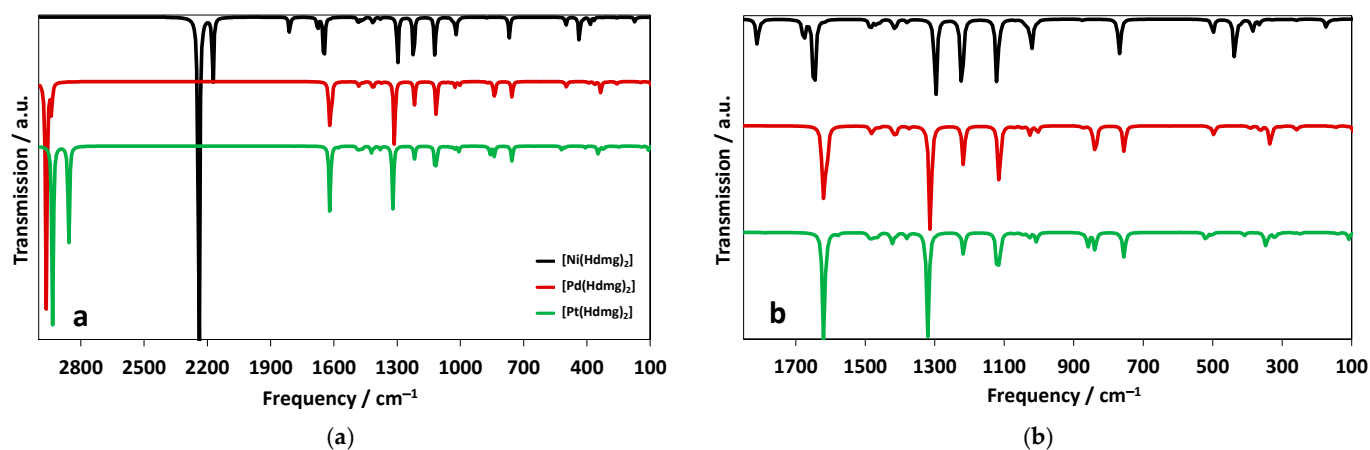


Figure 2. (a) DFT calculated IR spectra of $[\text{M}(\text{Hdmg})_2]$ ($\text{M} = \text{Ni}, \text{Pd}, \text{Pt}$), solvent: DMSO, functional: M06-2X, basis set: For C, H, N, O: def2TZVP, and for Ni, Pd, and Pt: LANL2DZ ecp. (b) Magnified view ($1850\text{--}100\text{ cm}^{-1}$) of the IR spectra of $[\text{M}(\text{Hdmg})_2]$ ($\text{M} = \text{Ni}, \text{Pd}, \text{Pt}$).

Table 1. Selected (experimental and computed) IR data for $[\text{Ni}(\text{Hdmg})_2]^a$.

O-H Stretching	O-H Bending	C=N Stretching	N-O Stretching	N-O Stretching	Reference
2174 (sym) 2240 (asym)	1810	1647 and 1677	1222 and 1297	1121	Our Calc.
2429 (sym) 2540 (asym)	1600–1823	1637	1336 (sym) 1365 (asym)	1261 (sym) 1261 (asym)	Calc. [1] ^b
2585	1782	1529 and 1590	1249	1120	Calc. [85] ^c
2350	1780	1560	1235	1100	Exp. [21]
2350	-	1576	1241	1103	Exp. [17]
-	1790	1550 and 1572	1240	1101	Exp. [87]

^a Calculated transition energies or observed band maxima in cm^{-1} . Our results: Solvent: DMSO, functional: M06-2X, basis set: def2TZVP for C, H, N, O, LANL2DZ ecp for Ni; Calc.: calculated data; Exp.: experimental data. ^b functional: ω B97X-D, basis sets 6-31G (d,p) for C, H, N, O and LANL2DZ ecp for Ni. ^c Functional: B3LYP, basis set: 6-311+(+)G**.

Table 2. Selected (experimental and computed) IR data for [Pd(Hdmg)₂]^a.

O-H	O-H	C=N	N-O	N-O	Reference
Stretching	Bending	Stretching	Stretching	Stretching	
2939 (sym) 2964 (asym)	1786	1611 and 1621	1217 and 1313	1114	Our results
2340	1710	1550 and 1500	1250	1090	Exp. [21]
2340	-	1552	1259	1091	Exp. [17]

^a Calculated transition energy or observed band maxima in cm⁻¹. Our results: Solvent: DMSO, functional: M06-2X, basis set: def2TZVP for C, H, N, O, LANL2DZ ecp for Pd; Exp.: experimental data.

Table 3. Selected (experimental and computed) IR data for [Pt(Hdmg)₂]^a.

O-H	O-H	C=N	N-O	N-O	Reference
Stretching	Bending	Stretching	Stretching	Stretching	
2857 (sym) 2934 (asym)	1788	1619	1217 and 1320	1119	Our results
2350	-	1550	1262	1089	Exp. [17]

^a Calculated transition energy or observed band maxima in cm⁻¹. Our results: Solvent: DMSO, functional: M06-2X, basis set: def2TZVP for C, H, N, O, LANL2DZ ecp for Pt; Exp.: experimental data.

Three transitions in the calculated spectra can be assigned to N–O stretching. They show very different intensities for the three complexes, while the energies are rather invariable (Figure 2, Tables 1–3).

For the C=N stretching modes the calculated spectra show two transitions for Ni (Table 1) and Pd (Table 2) and two merged bands for Pt (Table 3). They have similar intensities and similar energies for Pd and Pt but far higher values for Ni. We ascribe the energy differences between the metals to higher metal d to π^*_{CN} backbonding for Pt and Pd compared to Ni, in keeping with the larger 5d and 4d orbitals compared with 3d. The O–H bending vibrations showed a characteristic band in Ni complex at 1810 cm⁻¹, while for Pd and Pt complexes these transitions are extremely weak and at the same energy (1786 cm⁻¹).

The O–H symmetric and asymmetric stretching modes in the calculated IR spectra of [Ni(Hdmg)₂] are far lower (2174 and 2240 cm⁻¹) than those of [Pd(Hdmg)₂] (2939 and 2964 cm⁻¹) and [Pt(Hdmg)₂] (2857 and 2934 cm⁻¹) (Figure 2, Tables 1–3). The calculated values are perfectly in keeping with our calculated structural data and in line with increasing ionic radii for the metals (Pd²⁺ > Pt²⁺ >> Ni²⁺) [63–65,67] weakening the H bond. For the asymmetric O–H \cdots O interactions this would lead to a shorter O–H bond and higher frequency [86]. Akin to a recent theoretical study [1], we also found that the asymmetric O–H stretching vibration in comparison with the symmetric stretching is very intense. This is in line with the bigger change of molecular dipole moment for the asymmetric O–H stretching mode.

3.3. Energies and Compositions of the Frontier Orbitals

The energies and compositions of the lowest unoccupied molecular orbital (LUMO) and highest occupied molecular orbitals (HOMO) were calculated for the three complexes based on the *S*₀ and *T*₁ geometry-optimised structures (Figures S1–S3 and Tables S5–S7 in the Supplementary Materials). In the electronic *S*₀ ground state, most of the frontier orbitals including HOMO-3 to LUMO+3 differ from the Ni complex to the Pd and Pt derivatives, with the exception of the LUMOs which are highly similar in all three complexes with large coefficients on the metal-ligand bonds and the dmg π system (Figure 3 and Figure S2). The HOMO for the Ni complex is essentially centred on the ligands (100%) and has high similarities with the HOMO-1 for Pt (Figure 3), while the HOMO for the Pt complex obtains some metal d contributions (18%). For Pd these two orbitals are almost degenerate and the HOMO also obtains some metal contributions (8%). All three HOMO-3 orbitals have

predominant metal d_z^2 character with the d_z^2 character getting more and more dominant along the series Ni \ll Pd $<$ Pt. For all three complexes, the LUMO and LUMO+1 have small to negligible metal contributions. The LUMO+2 for Pt and the LUMO+3 for Pd resemble the essentially metal-centred LUMO+3 of the Ni complex (Figure S2) and clearly represent the metal p_z orbital.

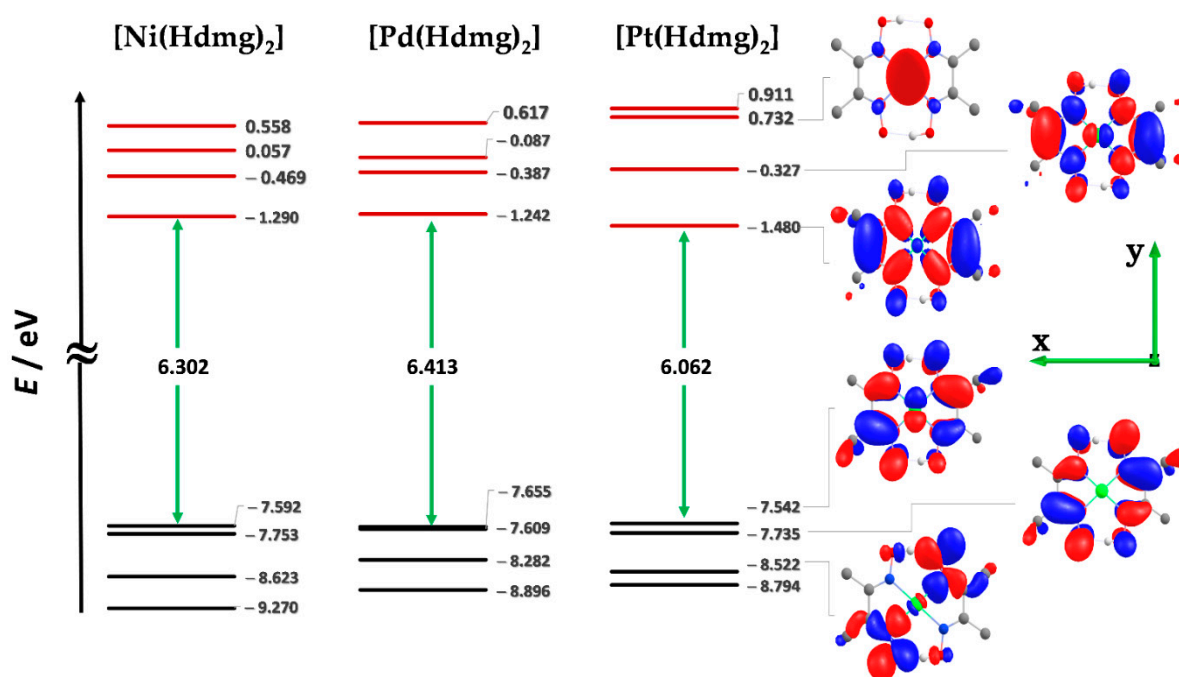


Figure 3. DFT calculated energies of occupied MOs (black) and unoccupied MOs (red) for [M(Hdmg)₂]; frontier MOs are given for M = Pt.

The calculated HOMO–LUMO energy gaps are 6.302 and 6.413 eV for the Ni and Pd complexes, respectively and reduced to 6.062 eV for the Pt complex, which is caused by a marked stabilisation of the LUMO (Figure 3). This series Pd $>$ Ni $>$ Pt agrees quite well with the experimental binding energies and electrochemical or optical HOMO–LUMO gaps of comparable series of Pt, Pd, and Ni complexes [63–65,67,77].

The XPS determined Ni 2p binding energies for [Ni(Hdmg)₂] are reported at about 853 (2p_{3/2}) to 870 (2p_{1/2}) eV [38] while for the ligands N(1s) and O(1s) binding energies the sequence is Pt \sim Pd $>$ Ni [91] which is in keeping with the size of the metal valence orbitals for the π -backbonding.

Gas-phase DFT calculations of [Ni(Hdmg)₂] gave a value of 7.32 eV decreasing to 6.97 eV upon dimerisation [1] and very similar HOMO and LUMO compositions. Adding one or two H₂O or NH₃ molecules as additional axial ligand increased the value for the monomer and also changed the orbital composition of HOMO and LUMO [1].

The frontier orbitals of the T_1 excited state (LSOMO: Lowest Singly Occupied Molecular Orbital, and HSOMO: Highest Singly Occupied Molecular Orbital) showed predominant contributions of the ligand to the HSOMO and HSOMO+1, while the metal participation increases in the LSOMO and LSOMO-1 for Pd and Pt complexes (Figure S3 and Table S7, Supplementary). So, again the Ni complex differs from the Pd and Pt derivatives. The HSOMO and LSOMO are mostly located in the ligand for Ni complex and metal contribution increases in the HSOMO+2 and HSOMO+3.

When comparing the HOMO–LUMO (S_0) and LSOMO–HSOMO (T_1) energy level diagrams for the three complexes (Figure S4, Supplementary) a significant stabilisation in the energy of the HSOMO compared with the LUMO is found, while the LSOMO for the T_1 state remained close to the HOMO of the S_0 state in all three cases.

3.4. UV-vis Absorption Spectroscopy

TD-DFT calculated absorption bands are very similar for all three complexes and show three main band systems containing several transitions (Figure 4). A closer look shows that the intense bands in the range 150–180 nm are very similar with maxima at 170, 171 and 176 nm for Ni(II), Pd(II), and Pt(II), respectively. The band system ranging from 180 to 280 nm shows more pronounced differences in energy (211, 231 and 250 nm) and band shape. The long-wavelength envelopes found from 270 to 400 nm are very similar for Ni and Pd, with maxima at 310 and 312 nm, respectively. For the Pt complex, the long-wavelength absorption is markedly red-shifted to the range 307–440 nm with a maximum of 350 nm. The intensity of these maxima decreases along the series from 6178 (Ni) to 4016 (Pd) and 2835 $\epsilon/\text{M}^{-1}\text{cm}^{-1}$ (Pt) (Table 4).

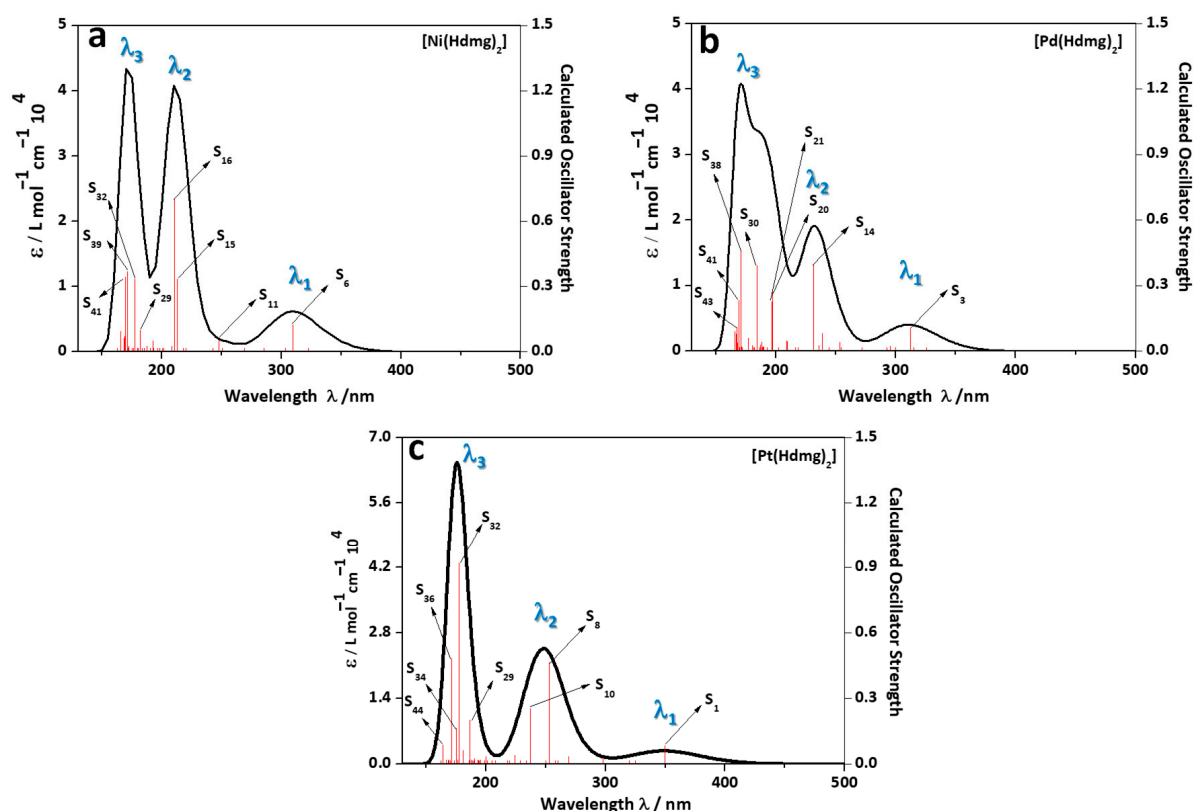


Figure 4. TD-DFT-calculated UV-vis absorption spectra of $[\text{Ni}(\text{Hdmg})_2]$ (a), $[\text{Pd}(\text{Hdmg})_2]$ (b), and $[\text{Pt}(\text{Hdmg})_2]$ (c), (solvent: DMSO, functional: M06-2X, basis set: def2TZVP For C, H, N, O, LANL2DZ ecp for Ni, Pd and Pt).

Table 4. DFT-calculated absorption maxima of the complexes $[\text{M}(\text{Hdmg})_2]$ (M = Ni, Pd, Pt) ^{a,b}.

$[\text{M}(\text{Hdmg})_2]$	$[\text{Ni}(\text{Hdmg})_2]$	$[\text{Pd}(\text{Hdmg})_2]$	$[\text{Pt}(\text{Hdmg})_2]$
λ_3 (ϵ) ^b	170 (4.3)	171 (4.1)	176 (6.5)
λ_2 (ϵ) ^b	211 (4.1)	231 (1.9)	250 (2.5)
λ_1 (ϵ) ^b	310 (6.2)	312 (4.0)	350 (2.8)

^a Solvent: DMSO, functional: M06-2X, basis set: For C, H, N, O: def2TZVP, for Ni, Pd, Pt: LANL2DZ ecp.

^b Absorption maxima λ are given in nm, and molar absorption coefficients ϵ are given in $10^4 \text{ L mol}^{-1} \text{ cm}^{-1}$.

The broad long-wavelength absorption band for $[\text{Ni}(\text{Hdmg})_2]$ is essentially composed of the HOMO-1 \rightarrow LUMO (79%) and HOMO \rightarrow LUMO+1 (12%) transitions (Table S8, Supplementary). The same band for the Pd complex correspond to a mixture of the HOMO-1 \rightarrow LUMO (48%) and HOMO \rightarrow LUMO (35%) transitions (Table S9). Visual plots of the molecular orbitals (Figure S1, SI) show that both bands have almost pure π - π^* character. For the Pt complex, this band is essentially described by the HOMO \rightarrow LUMO (90%) tran-

sition (Table S10) with has essentially ligand-centred $\pi-\pi^*$ character, but with a marked metal-to-ligand charge transfer (MLCT) contribution (Figure S1).

Further absorption bands at higher energy have predominant $\pi-\pi^*$ character which is in line with most of the states being essentially ligand centred (Figure S1 and Tables S6 and S7). Marked MLCT contributions for the Ni complex are found for transitions from HOMO-8 and HOMO-9 to the LUMO (Table S8). Corresponding transitions from the Pd and Pt derivatives include the HOMO-7 and HOMO-6 states, respectively (Tables S9 and S10). This is in line with the increasing ligand field energy and π -backbonding in the series Ni-Pd-Pt leading to a de-stabilisation of the low-lying $d\pi$ orbitals. No transitions with pronounced ligand field ($d-d^*$) character were found for the three complexes. However for Pd and Pt transitions with marked d-p character (HOMO-3 \rightarrow LUMO+3 (Pd) or HOMO-3 \rightarrow LUMO+2 (Pt)) were found at quite high energies corresponding to 167 and 181 nm for Pd and Pt, respectively. The p-type HOMO+3 orbital for Ni is less involved in electronic transitions.

The calculated spectra for [Pd(Hdmg)₂] and [Pt(Hdmg)₂] show the expected red-shifted bands compared with the Ni derivative (Table 4) in keeping with experimental spectra on all three complexes in CHCl₃ solution [15,16,57] and spectra recorded on thin films [27–30,51] or solids [22,51,57,92,93]. Also, the underlying transitions were quite similar for all three complexes as has been suggested before based on experimental data [17,27–30,51,90,93].

The recently calculated absorption spectra of monomeric and dimeric (Ni \cdots Ni stacked) [Ni(Hdmg)₂] are on first view similar to our spectrum absorption maxima [1]. A closer look shows that the energies of the two UV bands with maxima at 180 and 220 nm do not differ much between monomer and dimer. The calculated energies of these gas-phase calculations using the range-separated hybrid functional ω B97X-D, augmented with dispersion correction and split-valence 6-31G (d,p) basis set for all non-metallic elements and LANL2DZ ecp for Ni are only slightly lower than our numbers (Table 4). However, for the long-wavelength bands, this method gave a very different band maximum of 359 nm compared with 310 nm from our calculations in DMSO solvent and dimerisation shifted the band to 368 nm [1]. In the same study the long-wavelength band is described to have d-p character although their main contributions come from the HOMO-1 \rightarrow LUMO and HOMO-2 \rightarrow LUMO transitions [1] and their HOMO-1, HOMO-2 and LUMO show higher metal contributions than those calculated in our study.

Experimental UV-vis absorption spectra reported for [Ni(Hdmg)₂] in CHCl₃ solution showed pronounced bands at 253, 328, 373 and 420 nm [15,16,57] but also features at lower energies [16,57]. For other solvents, very similar absorptions were reported [16,17,46,52,57] and for the Pd and Pt derivatives, these bands are markedly red-shifted [57,92]. The bands ranging from 200 to 300 nm and the long-wavelength bands at 300–400 nm have been previously assigned to either $\pi-\pi^*$, MLCT or mixed $\pi-\pi^*/$ MLCT transitions [1,15–17,46,48,51,57,92,93]. Importantly, no solvatochromic effect was found on the spectra [Ni(Hdmg)₂] in solvents ranging from benzene to water [16] and a band at 266 nm is also observed for the Hdmg[−] anion in solution [17], which is rather counter-indicative for charge transfer transitions but supports the idea of solvent-invariant $\pi-\pi^*$ transitions [94,95].

In films and bulk solids broad absorption bands with maxima ranging from 500 to 700 nm dominate the visible part of the spectrum while the UV to visible part looks similar to the spectra in solution [15,16,46,57,92,93]. The broad long-wavelength bands were assigned to the so-called d-p ($3d_z^2 \rightarrow 4p_z$) transitions [1–3,6,15,46,48–52,57]. The energy of these transitions is very dependent on the metal \cdots metal proximity and stronger interactions lead to lower absorption energies [1–3,6,9,15,26–30,46–51,57]. The appearance of this band in studies reporting spectra of dissolved complexes is thus a clear indication for intermolecular stacking and formation of oligomeric stacks in such solutions [15,16,46,57]. This is strongly supported by the above mentioned calculated red-shift for a long-wavelength band for the Ni \cdots Ni stacked dimer [Ni(Hdmg)₂]₂ compared with the monomer while UV

are not affected from dimerisation [1]. This makes it also difficult to compare our calculated spectra with experimental data.

In summary, contrasting to previous assignments of the absorption bands ranging from 200 to 450 nm to essentially MLCT with some π - π^* character we found a predominant π - π^* character for all these bands. In contrast to previous studies, we also found that admixture of metal contributions of MLCT or d-p type occurs rather for transitions at higher energies, while the long-wavelength bands retain rather pure π - π^* character. However, this picture rapidly changes when axial ligands were added or dimers were formed [1,2]. Then metal-contributions both of MLCT and d-p type get more pronounced for the long-wavelength absorptions of the monomeric species and dominate for the stacked molecules in the solid the visible spectral range with the typical d-p transitions (mixed with MLCT type of transition) [1–3,6,15,46,48–52]. In our calculations, we used the conductor-like polarizable continuum model (CPCM) for the inclusion of polarisation effects from the solvent (here: DMSO). However, this method does not include real solvent molecules which are potentially coordinating but provides a polarisable surrounding (continuum). Compared with calculations on monomers in the gas phase [1] our calculation might thus overestimate delocalisation effects. However, our model definitely seems to be able to circumvent the dramatic impact of any species (ligands, other complexes) in the axial positions of the planar complexes on the d_z^2 and p_z orbitals leading to massive metal contributions to optical transitions.

4. Conclusions

We have studied the three Ni^{II}, Pd^{II} and Pt^{II} complexes [M(Hdmg)₂] (H₂dmg = dimethylglyoxime) by density functional DFT and TD-DFT methods to explore the structural and IR and UV-vis absorption spectroscopic properties of the molecular species of these complexes. The three compounds have a very high tendency to form metal···metal directed stacks and thus aggregate rapidly in solution. This has previously hampered spectroscopic characterisation of these complexes in solution and most of the studies, including theoretical studies, and most reported applications have been focussing on the solid-state. Still, some applications such as catalysis, trace element detection and biomedicine might be based on monomolecular species. Studies reporting spectroscopic properties of the complexes in solution are rare and mainly restricted to UV-vis absorption spectra. These studies reported bands in the visible range (>400 nm), but recent quantum chemical calculations did not agree with these observations and we supposed that instead of monomolecular species these solutions represent monomolecular together with oligomeric species. Thus, spectroscopic data of the monomolecular species is probably not reported yet. Thus, we computed the molecular geometries, IR spectra, frontier orbital compositions and energy together with UV-vis spectra using the M06-2X functional and LANL2DZ ecp (metals) and def2TZVP (other atoms) as basis sets. DMSO as solvent was included employing the conductor-like polarizable continuum model (CPCM). The optimised molecular geometries proved the asymmetric character of the two formed O–H···O bonds in the compounds, which connect the adjacent Hdmg[−] ligands in the completely planar complexes. IR frequencies of the O–H bond were higher in the Pd^{II} and Pt^{II} complexes than the Ni^{II} derivative in line with weaker H···O interactions. Comparison of calculated data of [M(Hdmg)₂] from three DFT studies showed that the use of split-valence basis sets is superior to the previously reported use of one type of basis sets for the metals and the light atoms (B3LYP functional and 6-311+(+)G**basis set). Calculated compositions of frontier orbitals gave essentially ligand-centred lowest unoccupied molecular orbitals (LUMOs) and highest occupied molecular orbitals (HOMO) except for the LUMO+3 (Ni, Pd) or LUMO+2 (Pt) with clear metal p_z and the HOMO-3 orbitals with predominant metal d_z^2 character. Calculated UV-vis spectra gave three bands in the range 180 to 350 nm. These bands are similar for all three complexes but show a marked red-shift in the series going from Ni to Pt. We assign them to predominantly ligand-centred π - π^* transitions, in contrast to previous assignments to mainly metal(d) to ligand(π^*) charge transfer (MLCT) transitions. For our calculations

metal contributions to the π - π^* transitions occur only at higher energies for the monomolecular species, while the long-wavelength bands have almost pure π - π^* character. These metal contributions comprise MLCT and also the notorious so-called d-p transitions that dominate the visible spectral range and the colours and other opto-electronic properties of the three compounds in the solid. Although, these d-p transitions have previously been assigned to absorption bands in the UV to vis range (200–450 nm) for the isolated molecules in solution, we found significant d-p contributions only for bands at around 180 nm for Pt and Pd and none for Ni. Other calculations on monomers, dimers and oligomers showed that further ligands added to the two axial positions, dimerisation or oligomerisation has a strong impact on both the $3d_z^2$ and the $4p_z$ orbitals dramatically increasing their contributions to the electronic transitions. Together with these calculations, our results support our idea that spectroscopic data of these three complexes does not represent the isolated molecules but a mixture of monomeric and oligomeric species. In a way, we looked for the first time at the isolated molecules in a surrounding-isolating solvent model.

Supplementary Materials: The following figures and tables are available online at <https://www.mdpi.com/article/10.3390/inorganics9060047/s1>. Table S1: Essential experimental structural parameters of $[M(\text{Hdmg})_2]$ ($M = \text{Ni, Pd, Pt}$). Table S2: Selected experimental and computed geometries of $[\text{Ni}(\text{Hdmg})_2]$, Table S3: Selected experimental and computed geometries of $[\text{Pd}(\text{Hdmg})_2]$, Table S4: Selected (experimental and computed) geometries of $[\text{Pt}(\text{Hdmg})_2]$, Figure S1: DFT-optimised structures in the S_0 ground state for $[M(\text{Hdmg})_2]$ ($M = \text{Ni, Pd, Pt}$), Table S5: The XYZ coordinates of the optimised ground state for $[M(\text{Hdmg})_2]$ ($M = \text{Ni, Pd, Pt}$), Table S6: Compositions (%) of frontier MOs in the S_0 ground state for $[M(\text{Hdmg})_2]$ ($M = \text{Ni, Pd, Pt}$), Figure S2: Frontier orbital landscape in the S_0 ground state for $[M(\text{Hdmg})_2]$ ($M = \text{Ni, Pd, Pt}$), Table S7: Compositions (%) of frontier MOs in the T_1 excited state for $[M(\text{Hdmg})_2]$ ($M = \text{Ni, Pd, Pt}$), Figure S3: Frontier orbital landscape in the T_1 excited state for $[M(\text{Hdmg})_2]$ ($M = \text{Ni, Pd, Pt}$), Figure S4: Energy diagrams of frontier MOs for $[M(\text{Hdmg})_2]$ ($M = \text{Ni, Pd, Pt}$) at the optimised S_0 and T_1 geometry, Table S8: Wavelengths and character of calculated transitions for $[\text{Ni}(\text{Hdmg})_2]$, Table S9: Wavelengths and character of calculated transitions for $[\text{Pd}(\text{Hdmg})_2]$, Table S10: Wavelengths and character of calculated transitions for $[\text{Pt}(\text{Hdmg})_2]$.

Author Contributions: M.N. carried out the DFT calculations, provided figures and tables and wrote the draft manuscript. A.K. supervised the project, did the data curation and revised the manuscript. Both authors have read and agreed to the published version of the manuscript.

Funding: M.N. acknowledges the German Academic Exchange Service (DAAD)—Funding programme/-ID: Research Grants—Doctoral Programmes in Germany, 2020/21 (grant No. 57507871).

Institutional Review Board Statement: Not applicable.

Informed Consent Statement: Not applicable.

Data Availability Statement: Not applicable.

Acknowledgments: We thank Simon Schmitz and Alexander Haseloer (both Department of Chemistry, University of Cologne) for support with the DFT calculations. The Regional Computing Centre of the University of Cologne (RRZK) is acknowledged for providing computing time on the DFT-funded High-Performance Computing (HPC) system CHEOPS as well as for the support.

Conflicts of Interest: The authors declare no conflict of interest.

References

1. Ali, S.Y.; Reddy, K.D.; Manna, A.K. Structural, Electronic, and Spectral Properties of Metal Dimethylglyoximate $[M(\text{DMG})_2]$; $M = \text{Ni}^{2+}, \text{Cu}^{2+}$ Complexes: A Comparative Theoretical Study. *J. Phys. Chem. A* **2019**, *123*, 9166–9174. [[CrossRef](#)] [[PubMed](#)]
2. Patra, S.G.; Mandal, N.; Datta, A.; Datta, D. On bonding in bis(dimethylglyoximate)nickel(II). *Comput. Theor. Chem.* **2017**, *1114*, 118–124. [[CrossRef](#)]
3. Liu, K.; Orimoto, Y.; Aoki, Y. Theoretical investigation of the pressure-induced insulator-to-metal-to-insulator transitions in one-dimensional bis(dimethylglyoximate) platinum(II), $\text{Pt}(\text{dmg})_2$. *Polyhedron* **2015**, *87*, 141–146. [[CrossRef](#)]
4. Bruce-Smith, I.F.; Zakharov, B.A.; Stare, J.; Boldyreva, E.V.; Pullham, C.R. Structural Properties of Nickel Dimethylglyoxime at High Pressure: Single-Crystal X-ray Diffraction and DFT Studies. *J. Phys. Chem. C* **2014**, *118*, 24705–24713. [[CrossRef](#)]

5. Kovacs, A. Theoretical study of the strong intramolecular hydrogen bond and metal–ligand interactions in group 10 (Ni, Pd, Pt) bis(dimethylglyoximate) complexes. *J. Organomet. Chem.* **2007**, *692*, 5383–5389. [[CrossRef](#)]
6. Di Bella, S.; Casarin, M.; Fragala, I.; Granozzi, G.; Marks, T.J. Electronic Structure of Tetracoordinate Transition-Metal Complexes. 2. Comparative Theoretical ab Initio/Hartree-Fock-Slater and UV-Photoelectron Spectroscopic Studies of Building Blocks for Low-Dimensional Conductors: Glyoximate Complexes of Palladium(II) and Platinum(II). *Inorg. Chem.* **1988**, *27*, 3993–4002.
7. Yoshida, K. Epitaxial Growth of Bis(dimethylglyoximate)platinum(II) Accompanied by Hole Formation. *Cryst. Growth Des.* **2020**, *20*, 7271–7275. [[CrossRef](#)]
8. Takeda, K.; Sasaki, T.; Hayashi, J.; Kagami, S.; Shirotani, I.; Yakushi, K. X-ray and optical studies of one-dimensional bis(dimethylglyoximate)Pd(II), Pd(dmg)₂ at high pressures. *J. Phys. Conf. Ser.* **2010**, *215*, 012065. [[CrossRef](#)]
9. Thomas, T.W.; Underhill, A.E. Metal–metal interactions in transition-metal complexes containing infinite chains of metal atoms. *Chem. Soc. Rev.* **1972**, *1*, 99–120. [[CrossRef](#)]
10. Tazdher, G.; Dreos, R.; Felluga, A.; Nardin, G.; Randaccio, L.; Stener, M. Intramolecular and intermolecular O–H–O hydrogen bond in some nickel(II) complexes with tridentate amino-oxime ligands. *Inorg. Chim. Acta* **2003**, *355*, 361–367. [[CrossRef](#)]
11. Li, D.-X.; Xu, D.-J.; Xu, Y.-Z. Redetermination of bis(dimethylglyoximate- $[\kappa]^2-N,N'$)nickel(II). *Acta Crystallogr. Sect. E Struct. Rep. Online* **2003**, *59*, m1094–m1095. [[CrossRef](#)]
12. Konno, M.; Okamoto, T.; Shirotani, I. Structure changes and proton transfer between O···O in bis(dimethylglyoximate)platinum(II) at low temperature (150 K) and at high pressures (2.39 and 3.14 GPa). *Acta Crystallogr. Sect. B Struct. Sci.* **1989**, *45*, 142–147. [[CrossRef](#)]
13. Hussain, M.S.; Salinas, B.E.V.; Schlemper, E.O. Three-dimensional determinations of the crystal structures of bis(dimethylglyoximate)palladium(II) and bis(dimethylglyoximate)platinum(II). *Acta Crystallogr. Sect. B Struct. Crystallogr. Cryst. Chem.* **1979**, *35*, 628–633. [[CrossRef](#)]
14. Murmann, R.K.; Schlemper, E.O. On the crystal structure of bis(glyoximate)nickel(II). *Acta Crystallogr.* **1967**, *23*, 667–669. [[CrossRef](#)]
15. Martin, J.D.; Hogan, P.; Abboud, K.A.; Dahmen, K.-H. Variations on Nickel Complexes of the vic-Dioximes: An Understanding of Factors Affecting Volatility toward Improved Precursors for Metal–Organic Chemical Vapor Deposition of Nickel. *Chem. Mater.* **1998**, *10*, 2525–2532. [[CrossRef](#)]
16. Caton, J.E.; Banks, C.V. Studies of the spectra of copper dimethyl-glyoxime, nickel dimethylglyoxime and nickel ethylmethylglyoxime in various solvents. *Talanta* **1966**, *13*, 967–977. [[CrossRef](#)]
17. Burger, K.; Ruff, I.; Ruff, F. Some theoretical and practical problems in the use of organic reagents in chemical analysis—IV: Infra-red and ultra-violet spectrophotometric study of the dimethylglyoxime complexes of transition metals. *J. Inorg. Nucl. Chem.* **1965**, *27*, 179–190. [[CrossRef](#)]
18. Frasson, E.; Panattoni, C. X-ray studies on the metal complexes with the glyoximes. IV. Structure of Ni-methyl-ethyl-glyoxime. *Acta Crystallogr.* **1960**, *13*, 893–898. [[CrossRef](#)]
19. Williams, D.E.; Wohlaer, G.; Rundle, R.E. Crystal Structures of Nickel And Palladium Dimethylglyoximes. *J. Am. Chem. Soc.* **1959**, *81*, 755–756. [[CrossRef](#)]
20. Frasson, E.; Panattoni, C.; Zannetti, R. X-ray studies on the metal complexes with the glyoximes. II. Structure of the Pt-dimethylglyoxime. *Acta Crystallogr.* **1959**, *12*, 1027–1031. [[CrossRef](#)]
21. Blinc, R.; Hadži, D. Infrared spectra and hydrogen bonding in the nickel–dimethylglyoxime and related complexes. *J. Chem. Soc.* **1958**, 4536–4540. [[CrossRef](#)]
22. Huila, M.F.G.; Lukin, N.; Parussulo, A.L.A.; Oliveira, P.V.; Kyohara, P.K.; Araki, K.; Toma, H.E. Unraveling the Mysterious Role of Palladium in Feigl bis(dimethylglyoximate)nickel(II) Spot Tests by Means of Confocal Raman Microscopy. *Anal. Chem.* **2012**, *84*, 3067–3069. [[CrossRef](#)]
23. Sharpe, A.G.; Wakefield, D.B. The basis of the selectivity of dimethylglyoxime as a reagent in gravimetric analysis. *J. Chem. Soc.* **1957**, 281–285. [[CrossRef](#)]
24. Godycki, L.E.; Rundle, R.E. The structure of nickel dimethylglyoxime. *Acta Crystallogr.* **1953**, *6*, 487–495. [[CrossRef](#)]
25. Gerasimchuk, N. Editorial (Thematic Issue: Recent Advances in Chemistry and Applications of Oximes and their Metal Complexes: Part I). *Curr. Inorg. Chem.* **2015**, *5*, 3–4. [[CrossRef](#)]
26. Takeda, K.; Shirotani, I.; Yakushi, K. Pressure-Induced Insulator-to-Metal-to-Insulator Transitions in One-Dimensional Bis(dimethylglyoximate)platinum(II), Pt(dmg)₂. *Chem. Mater.* **2000**, *12*, 912–916. [[CrossRef](#)]
27. Shirotani, I.; Suzuki, K.; Yagi, T. Pressure-sensitive Optical Properties of Bis(1,2-dionedioximate)-Palladium(II) Complexes. *Proc. Jpn. Acad. Ser. B* **1992**, *68*, 57–62. [[CrossRef](#)]
28. Takeda, K.; Hayashi, J.; Shirotani, I.; Fukuda, H.; Yakushi, K. Structural, Optical, and Electrical Properties of One-Dimensional Bis(Dimethylglyoximate)nickel(II), Ni(dmg)₂ at High Pressure. *Mol. Cryst. Liq. Cryst.* **2006**, *460*, 131–144. [[CrossRef](#)]
29. Shirotani, I.; Suzuki, K.; Suzuki, T.; Yagi, T.; Tanaka, M. Absorption Spectra and Electrical Resistivities of Bis(1,2-dione dioximate)nickel(II) Complexes at High Pressures. *Bull. Chem. Soc. Jpn.* **1992**, *65*, 1078–1083. [[CrossRef](#)]
30. Shirotani, I.; Inagaki, Y.; Utsumi, W.; Yagi, T. Pressure-sensitive absorption spectra of thin films of bis(diphenylglyoximate)platinum(II), Pt(dpg)₂: Potential application as an indicator of pressure. *J. Mater. Chem.* **1991**, *1*, 1041–1043. [[CrossRef](#)]
31. Ferraro, J.R. Some possible new internal pressure calibrants. *Inorg. Nucl. Chem. Lett.* **1970**, *6*, 823–825. [[CrossRef](#)]

32. Kamnoet, P.; Aeungmaitrepirom, W.; Menger, R.F.; Henry, C.S. Highly selective simultaneous determination of Cu(II), Co(II), Ni(II), Hg(II), and Mn(II) in water samples using microfluidic paper-based analytical de-vices. *Analyst* **2021**, *146*, 2229–2239. [[CrossRef](#)]
33. Mirhashemi, A.; Ghorbani, Y.; Sadighi, S. Synthesis and evaluation of Fe₃O₄-Al₂O₃/SDS-DMG adsorbent for extraction and preconcentration of Pd(II) from real samples. *J. Iran. Chem. Soc.* **2020**, *17*, 2073–2081. [[CrossRef](#)]
34. Olorundare, F.O.G.; Nkosi, D.; Arotiba, O.A. Voltammetric Determination of Nitrophenols at a Nickel Dimethylglyoxime Complex—Gold Nanoparticle Modified Glassy Carbon Electrode. *Int. J. Electrochem. Sci.* **2016**, *11*, 7318–7332. [[CrossRef](#)]
35. Andris, B.; Prazsky, M.; Sebesta, F. Rapid separation and determination of ¹⁰⁷Pd in radioactive waste produced during NPP A-1 decommissioning. *J. Radioanal. Nucl. Chem.* **2015**, *304*, 123–126. [[CrossRef](#)]
36. Ma, J.; Meng, W.; Zhang, L.; Li, F.; Li, T. Effective oil–water mixture separation and photocatalytic dye de-contamination through nickel-dimethylglyoxime microtubes coated superhydrophobic and superoleophilic films. *RSC Adv.* **2021**, *11*, 5035–5043. [[CrossRef](#)]
37. Qi, P.; Gu, Y.; Sun, H.; Lian, Y.; Yuan, X.; Hu, J.; Deng, Z.; Yao, H.-C.; Guo, J.; Peng, Y. Active Nickel Derived from Coordination Complex with Weak Inter-/Intra-molecular Interactions for Efficient Hydrogen Evolution via a Tandem Mechanism. *J. Catal.* **2020**, *389*, 29–37. [[CrossRef](#)]
38. Sarkar, B.; Kwek, W.; Verma, D.; Kim, J. Effective vacuum residue upgrading using sacrificial nickel(II) dimethylglyoxime complex in supercritical methanol. *Appl. Catal. A Gen.* **2017**, *545*, 148–158. [[CrossRef](#)]
39. Titova, Y.Y.; Belykh, L.B.; Shmidt, F.K. Formation and properties of Ziegler systems based on nickel bis(dimethylglyoximate) in catalysis of hydrogenation reactions. *Russ. J. Gen. Chem.* **2014**, *84*, 2413–2420. [[CrossRef](#)]
40. Feng, J.-J.; Zhou, D.-L.; Xi, H.-X.; Chen, J.-R.; Wang, A.-J. Facile synthesis of porous worm-like Pd nanotubes with high electrocatalytic activity and stability towards ethylene glycol oxidation. *Nanoscale* **2013**, *5*, 6754–6757. [[CrossRef](#)] [[PubMed](#)]
41. Yuan, M.; Li, Q.; Zhang, J.; Wu, J.; Zhao, T.; Liu, Z.; Zhou, L.; He, H.; Li, B.; Zhang, G. Engineering Surface Atomic Architecture of NiTe Nanocrystals Toward Efficient Electrochemical N₂ Fixation. *Adv. Funct. Mater.* **2020**, *30*, 2004208. [[CrossRef](#)]
42. Wang, T.; Li, F.; Huang, H.; Yin, S.; Chen, P.; Jin, P.; Chen, Y. Porous Pd-PdO Nanotubes for Methanol Electrooxidation. *Adv. Funct. Mater.* **2020**, *30*, 2000534. [[CrossRef](#)]
43. Dong, X.; Li, J.; Wei, D.; Li, R.; Qu, K.; Wang, L.; Xu, S.; Kang, W.; Li, H. Pd(II)/Ni(II)-dimethylglyoxime derived Pd-Ni-P@N-doped carbon hybrid nanocatalysts for oxygen reduction reaction. *Appl. Surf. Sci.* **2019**, *479*, 273–279. [[CrossRef](#)]
44. Kordatos, K.; Vlasopoulos, A.; Strikos, S.; Ntziouni, A.; Gavela, S.; Trasobares, S.; Kasselouri-Rigopoulou, V. Synthesis of carbon nanotubes by pyrolysis of solid Ni(dm_g)₂. *Electrochim. Acta* **2009**, *54*, 2466–2472. [[CrossRef](#)]
45. Dakhel, A.; Ali-Mohamed, A.Y. Characterisation and ac-electrical investigation of sublimated bis(dimethylglyoximate)palladium(II) thin films. *J. Organomet. Chem.* **2006**, *691*, 3760–3764. [[CrossRef](#)]
46. Dakhel, A.A.; Ahmed, Y.A.-M.; Henari, F. Structural and optical studies of evaporated bis(dimethylglyoximate)nickel(II) thin films. *Opt. Mater.* **2006**, *28*, 925–929. [[CrossRef](#)]
47. Suzuki, I.; Honjo, T.; Terada, K. Vacuum Sublimation Behavior of Nickel(II), Palladium(II), and Platinum(II) Chelates with Dimethylglyoxime. *Bull. Chem. Soc. Jpn.* **1990**, *63*, 3686–3688. [[CrossRef](#)]
48. Iwai, S.; Kamata, T.; Murata, S.; Yamamoto, K.; Ohta, T. Wavepacket motion during thermalization of self-trapped exciton driven by an intramolecular vibration in one-dimensional platinum dimethylglyoxime complex. *J. Lumin.* **2000**, *87–89*, 629–632. [[CrossRef](#)]
49. Kamata, T.; Fukaya, T.; Matsuda, H.; Mizukami, F. Reversible control of the nonlinear optical activity of one-dimensional metal complexes. *Appl. Phys. Lett.* **1994**, *65*, 1343–1345. [[CrossRef](#)]
50. Kamata, T.; Curran, S.; Roth, S.; Fukaya, T.; Matsuda, H.; Mizukami, F. Third-order nonlinear optical properties of evaporated thin films of platinum-alkyldionedioxime complexes: Effects of metal—Metal distance. *Synth. Met.* **1996**, *83*, 267–271. [[CrossRef](#)]
51. Kamata, T.; Fukaya, T.; Kodzasa, T.; Matsuda, H.; Mizukami, F. Third-order nonlinear optical properties of bis(dimethylglyoximate)metal(II). *Synth. Met.* **1995**, *71*, 1725–1726. [[CrossRef](#)]
52. Yang, B.; Li, J.; Zhang, L.; Xu, G. A molecularly imprinted electrochemiluminescence sensor based on the mimetic enzyme catalytic effect for ultra-trace Ni₂₊ determination. *Analyst* **2016**, *141*, 5822–5828. [[CrossRef](#)] [[PubMed](#)]
53. Benoit, S.L.; Maier, R.J. The nickel-chelator dimethylglyoxime inhibits human amyloid beta peptide in vitro aggregation. *Sci. Rep.* **2021**, *11*, 1–11. [[CrossRef](#)] [[PubMed](#)]
54. Biancalana, L.; Batchelor, L.K.; Dyson, P.J.; Zacchini, S.; Schoch, S.; Pampaloni, G.; Marchetti, F. α -Diimine homologues of cisplatin: Synthesis, speciation in DMSO/water and cytotoxicity. *New J. Chem.* **2018**, *42*, 17453–17463. [[CrossRef](#)]
55. Kluge, T.; Bette, M.; Ruffer, T.; Bruhn, C.; Wagner, C.; Ströhl, D.; Schmidt, J.; Steinborn, D. Activation of Acetyl Ligands through Hydrogen Bonds: A New Way to Platinum(II) Complexes Bearing Protonated Imino-acetyl Ligands. *Organometallics* **2013**, *32*, 7090–7106. [[CrossRef](#)]
56. Schwieger, S.; Heinemann, F.W.; Wagner, C.; Kluge, R.; Damm, C.; Israel, G.; Steinborn, D. A Bis(acetyl)-Bridged Platinum(II) Coordination Polymer as a Building Block for Diacetylplatinum(II) Complexes and Platina- β -diketones. *Organometallics* **2009**, *28*, 2485–2493. [[CrossRef](#)]
57. Nagakura, S.; Ohashi, Y.; Hanazaki, I. Spectroscopic study of the interaction between the central metal ions in the crystals of bis(dimethylglyoximate)nickel(II) and related complexes. *Inorg. Chem.* **1970**, *9*, 2551–2556. [[CrossRef](#)]

58. Kurz, H.; Schötz, K.; Papadopoulos, I.; Heinemann, F.W.; Maid, H.; Guldi, D.M.; Hörner, G.; Weber, B. A Fluorescence-Detected Coordination-Induced Spin State Switch. *J. Am. Chem. Soc.* **2021**, *143*, 3466–3480. [[CrossRef](#)]
59. Berkefeld, A.; Fröhlich, M.; Kordan, M.; Hörner, G.; Schubert, H. Selective metalation of phenol-type proligands for preparative organometallic chemistry. *Chem. Commun.* **2020**, *56*, 3987–3990. [[CrossRef](#)]
60. Heil, A.; Marian, C.M. Structure—Emission Property Relationships in Cyclometalated Pt(II) β -Diketonate Complexes. *Inorg. Chem.* **2019**, *58*, 6123–6136. [[CrossRef](#)]
61. Garbe, S.; Krause, M.; Klimpel, A.; Neundorf, I.; Lippmann, P.; Ott, I.; Brünkink, D.; Strassert, C.A.; Doltsinis, N.L.; Klein, A. Cyclometalated Pt Complexes of CNC Pincer Ligands: Luminescence and Cytotoxic Properties. *Organometallics* **2020**, *39*, 746–756. [[CrossRef](#)]
62. Föllner, J.; Friese, D.H.; Riese, S.; Kaminski, J.M.; Metz, S.; Schmidt, D.; Wuerthner, F.; Lambert, C.; Marian, C.M. On the photophysical properties of Ir^{III}, Pt^{II}, and Pd^{II} (phenylpyrazole) (phenyldipyrin) complexes. *Phys. Chem. Chem. Phys.* **2020**, *22*, 3217–3233. [[CrossRef](#)]
63. Mews, N.M.; Reimann, M.; Hörner, G.; Kaupp, M.; Schubert, H.; Berkefeld, A. A four-parameter system for rationalising the electronic properties of transition metal–radical ligand complexes. *Dalton Trans.* **2020**, *49*, 9735–9742. [[CrossRef](#)] [[PubMed](#)]
64. Haseloer, A.; Denkler, L.M.; Jordan, R.; Reimer, M.; Olthof, S.; Schmidt, I.; Meerholz, K.; Hörner, G.; Klein, A. Ni, Pd, and Pt complexes of a tetradentate dianionic thiosemicarbazone-based O⁻N⁻N⁻S ligand. *Dalton Trans.* **2021**, *50*, 4311–4322. [[CrossRef](#)] [[PubMed](#)]
65. Eskelinen, T.; Buss, S.; Petrovskii, S.K.; Grachova, E.V.; Krause, M.; Klein, A.; Strassert, C.A.; Koshevoy, I.O.; Hirva, P. Photophysics and Excited State Dynamics of Cyclometalated [M(C⁻N⁻N)(CN)] (M = Ni, Pd, Pt) Complexes: A Theoretical and Experimental Study. *Inorg. Chem.* **2021**. [[CrossRef](#)]
66. Krause, M.; von der Stück, R.; Brünkink, D.; Buss, S.; Doltsinis, N.L.; Strassert, C.A.; Klein, A. Platinum and palladium complexes of tridentate ⁻C⁻N⁻N (phen-ide)-pyridine-thiazol ligands—A case study involving spectroelectrochemistry, photoluminescence spectroscopy and TD-DFT calculations. *Inorg. Chim. Acta* **2021**, *518*, 120093. [[CrossRef](#)]
67. Poirier, S.; Lynn, H.; Reber, C. Variation of M–H–C Interactions in Square-Planar Complexes of Nickel(II), Palladium(II), and Platinum(II) Probed by Luminescence Spectroscopy and X-ray Diffraction at Variable Pressure. *Inorg. Chem.* **2018**, *57*, 7713–7723. [[CrossRef](#)]
68. Frisch, M.J.; Trucks, G.W.; Schlegel, H.B.; Scuseria, G.E.; Robb, M.A.; Cheeseman, J.R.; Scalmani, G.; Barone, V.; Mennucci, B.; Petersson, G.A.; et al. *Gaussian 09, revision A.02*; Gaussian, Inc.: Wallingford, CT, USA, 2016.
69. Barone, V.; Cossi, M.; Tomasi, J. A new definition of cavities for the computation of solvation free energies by the polarizable continuum model. *J. Chem. Phys.* **1997**, *107*, 3210–3221. [[CrossRef](#)]
70. Cossi, M.; Scalmani, G.; Rega, N.; Barone, V. New developments in the polarizable continuum model for quantum mechanical and classical calculations on molecules in solution. *J. Chem. Phys.* **2002**, *117*, 43–54. [[CrossRef](#)]
71. Zhao, Y.; Truhlar, D.G. The M06 suite of density functionals for main group thermochemistry, thermochemical kinetics, noncovalent interactions, excited states, and transition elements: Two new functionals and systematic testing of four M06-class functionals and 12 other functionals. *Theor. Chem. Acc.* **2008**, *120*, 215–241. [[CrossRef](#)]
72. Weigend, F.; Ahlrichs, R. Balanced basis sets of split valence, triple zeta valence and quadruple zeta valence quality for H to Rn: Design and assessment of accuracy. *Phys. Chem. Chem. Phys.* **2005**, *7*, 3297–3305. [[CrossRef](#)]
73. Roy, L.E.; Hay, P.J.; Martin, R.L. Revised Basis Sets for the LANL Effective Core Potentials. *J. Chem. Theory Comput.* **2008**, *4*, 1029–1031. [[CrossRef](#)] [[PubMed](#)]
74. Röhlfing, C.M.; Hay, P.J.; Martin, R.L. An effective core potential investigation of Ni, Pd, and Pt and their monohydrides. *J. Chem. Phys.* **1986**, *85*, 1447–1455. [[CrossRef](#)]
75. Hay, P.J.; Wadt, W.R. Ab initio effective core potentials for molecular calculations. Potentials for K to Au including the outermost core orbitals. *J. Chem. Phys.* **1985**, *82*, 299–310. [[CrossRef](#)]
76. Hay, P.J.; Wadt, W.R. Ab initio effective core potentials for molecular calculations. Potentials for the transition metal atoms Sc to Hg. *J. Chem. Phys.* **1985**, *82*, 270–283. [[CrossRef](#)]
77. Potocny, A.M.; Pistner, A.J.; Yap, G.P.A.; Rosenthal, J. Electrochemical, Spectroscopic, and ¹O₂ Sensitization Characteristics of Synthetically Accessible Linear Tetrapyrrole Complexes of Palladium and Platinum. *Inorg. Chem.* **2017**, *56*, 12703–12711. [[CrossRef](#)]
78. Kar, P.; Yoshida, M.; Kobayashi, A.; Routaboul, L.; Braunstein, P.; Kato, M. Colour tuning by the stepwise synthesis of mononuclear and homo- and hetero-dinuclear platinum(II) complexes using a zwitterionic quinonoid ligand. *Dalton Trans.* **2016**, *45*, 14080–14088. [[CrossRef](#)]
79. Phadnis, P.P.; Jain, V.K.; Schurr, T.; Klein, A.; Lissner, F.; Schleid, T.; Kaim, W. Synthesis, spectroscopy, structure and photophysical properties of dinaphthylmethylarsine complexes of palladium(II) and platinum(II). *Inorg. Chim. Acta* **2005**, *358*, 2609–2617. [[CrossRef](#)]
80. Dey, D.; Kumbhare, L.B.; Jain, V.K.; Klein, A.; Schurr, T.; Kaim, W.; Belaj, F. Structural Varieties in 1-Dimethylaminopropyl-2-chalcogenolate and 2-Dimethylaminopropyl-1-chalcogenolate (S, Se, Te) Complexes of Palladium(II) and Platinum(II): Synthesis, Spectroscopy and Structures. *Eur. J. Inorg. Chem.* **2004**, *22*, 4510–4520. [[CrossRef](#)]
81. Phadnis, P.P.; Jain, V.K.; Klein, A.; Weber, M.; Kaim, W. Configurational selectivity in benzyldimethylarsine complexes of palladium(II) and platinum(II): Synthesis, spectroscopy and structures. *Inorg. Chim. Acta* **2003**, *346*, 119–128. [[CrossRef](#)]

82. Huheey, J.E.; Huheey, C.L. Anomalous properties of elements that follow “long periods” of elements. *J. Chem. Educ.* **1972**, *49*, 227–230. [[CrossRef](#)]
83. Steiner, T. The Hydrogen Bond in the Solid State. *Angew. Chem. Int. Ed.* **2002**, *41*, 48–76. [[CrossRef](#)]
84. Rundle, R.E.; Parasol, M. O–H Stretching Frequencies in Very Short and Possibly Symmetrical Hydrogen Bonds. *J. Chem. Phys.* **1952**, *20*, 1487–1488. [[CrossRef](#)]
85. Caton, J.E.; Banks, C.V. Hydrogen bonding in some copper(II) and nickel(II) *vic*-dioximes. *Inorg. Chem.* **1967**, *6*, 1670–1675. [[CrossRef](#)]
86. Orel, B.; Penko, M.; Hadzi, D. Infrared and resonance enhanced Raman spectra of some metal *vic*-dioximes with short hydrogen bonds. *Spectrochim. Acta Part A Mol. Spectrosc.* **1980**, *36*, 859–864. [[CrossRef](#)]
87. Szabó, A.; Kovács, A. Vibrational analysis of the bis(dimethylglyoximate)nickel(II) complex. *J. Mol. Struct.* **2003**, *651–653*, 547–553. [[CrossRef](#)]
88. Várhelyi, C.; Kovács, A.; Gömör, A.; Várhelyi, C.; Pokol, G.; Farkas, G.; Sohár, P. Comparative spectral and thermal studies of [Pt(DioxH)₂] chelates. *J. Coord. Chem.* **2009**, *62*, 2429–2437. [[CrossRef](#)]
89. Bigotto, A.; Galasso, V.; De Alti, G. Infrared spectra of transition metal glyoximates. *Spectrochim. Acta Part A Mol. Spectrosc.* **1971**, *27*, 1659–1670. [[CrossRef](#)]
90. Kohler, U.; Hausen, H.-D.; Weidlein, J. Bis(dimethylmetall(III)glyoximate)metallate(II) (metall(III) = Al, Ga, In, metall(II) = Ni, Pd, Pt, Cu). *J. Organomet. Chem.* **1984**, *272*, 337–350. [[CrossRef](#)]
91. Yoshida, T. An X-Ray Photoelectron Spectroscopic Study of Dioxime Metal Complexes. *Bull. Chem. Soc. Jpn.* **1978**, *51*, 3257–3260. [[CrossRef](#)]
92. Basu, G.; Cook, G.M.; Belford, R.L. The Green Band of Crystalline Nickel Dimethylglyoxime. I. Mixed Crystals with Palladium, Platinum, and Copper and the Questions of Nonlocalized or d-p Transitions. *Inorg. Chem.* **1964**, *3*, 1361–1368. [[CrossRef](#)]
93. Nishida, Y.; Kozuka, M.; Nakamoto, K. Resonance raman spectra of [Ni(dm_g)₂], [Pd(dm_g)₂] and [Pt(dm_g)₂] in the solid state (dm_gH = dimethylglyoxime). *Inorg. Chim. Acta* **1979**, *34*, L273–L275. [[CrossRef](#)]
94. Kaim, W.; Kohlmann, S.; Ernst, S.; Olbrich-Deussner, B.; Bessenbacher, C.; Schulz, A. What determines the solvatochromism of metal-to-ligand charge transfer transitions? A demonstration involving 17 tungsten carbonyl complexes. *J. Organomet. Chem.* **1987**, *321*, 215–226. [[CrossRef](#)]
95. Manuta, D.M.; Lees, A.J. Solvatochromism of the Metal to Ligand Charge-Transfer Transitions of Zerovalent Tungsten Carbonyl Complexes. *Inorg. Chem.* **1986**, *25*, 3212–3218. [[CrossRef](#)]